The predominance of substrate induced defects in magnetic properties of Sr_2FeMoO_6 thin films

2015 J. Phys.: Condens. Matter 27 386001

(http://iopscience.iop.org/0953-8984/27/38/386001)

IOP Publishing Journal of Physics: Condensed Matter
J. Phys.: Condens. Matter **27** (2015) 386001 (11pp) doi:10.1088/0953-8984/27/38/386001

The predominance of substrate induced defects in magnetic properties of Sr_2FeMoO_6 thin films

M Saloaro[1], H Deniz[2], H Huhtinen[1], H Palonen[1], S Majumdar[1,3] and P Paturi[1]

[1] Wihuri Physical Laboratory, Department of Physics and Astronomy, FI-20014 University of Turku, Finland
[2] Max Planck Institute of Microstructure Physics, Weinberg 2, 06120 Halle, Germany
[3] NanoSpin, Department of Applied Physics, Aalto University School of Science, PO Box, FI-00076 Aalto, Finland

E-mail: minnamari.saloaro@utu.fi

Received 28 May 2015, revised 24 July 2015
Accepted for publication 12 August 2015
Published 4 September 2015

Abstract

A systematic study of epitaxially grown Sr_2FeMoO_6 thin films on $SrTiO_3$, $(LaAlO_3)_{0.3}$ $(Sr_2AlTaO_6)_{0.7}$, $SrLaAlO_4$ and MgO single crystal substrates were made. Transmission electron microscopy investigations showed sharp substrate/films interfaces and increased defect concentration with increased lattice mismatch, indicating defect formation such as dislocations, low angle grain boundaries and stacking faults as a strain relaxation mechanism. Large enough compressive mismatch cause the over-relaxation of the lattice parameters through reorganization or interface defects, which was observed as a tensile strain in films with compressive mismatch larger than −1.05%. All the films with compressive mismatch were phase pure and epitaxially textured while signatures of $SrMoO_4$ parasitic particle was found only in the film grown on MgO. No correlation between the antisite disorder and other structural defects or magnetic properties were found. Instead, the saturation magnetization, Curie temperature, magnetic domain rotation etc are higly dependent on the lattice mismatch induced defects, which outshines the possible correlation with B-site ordering.

Keywords: Sr_2FeMoO_6, thin films, substrates, antisite disorder, TEM, defects, magnetic properties

(Some figures may appear in colour only in the online journal)

1. Introduction

The novel spintronic applications for future information technology need high quality thin films of multifunctional materials that possess required features at room temperature. In addition to the manganites and magnetic semiconductors, one of the potential materials is the $A_2BB'O_6$-type double perovskite Sr_2FeMoO_6 (SFMO), which has a large magnetoresistance as an intrinsic property and 100% spin polarized charge carriers. The Curie temperature, T_C, of SFMO is around 410–450 K [1], which is exceptionally high among half metals and enables room temperature applications.

High quality SFMO thin films have been mostly grown with pulsed laser deposition (PLD) on single crystal substrates, but several other fabrication methods have also been used [2–8]. The most common substrate for the growth of SFMO is the $SrTiO_3$ [9–13]. However, the structural and magnetic properties of SFMO films on several different substrates including $LaAlO_3$ and MgO have been reported [14–18]. The x-ray diffraction (XRD) and atomic force microscopy (AFM) studies of the pulsed laser deposited SFMO thin films by Jalili *et al* have suggested different growth mechanisms for the SFMO films grown on $SrTiO_3$, MgO and $LaAlO_3$ substrates at 800 °C [16]. The surface morphology indicated a layer-by-layer

growth on $SrTiO_3$ and MgO, whereas three-dimensional progressive growth is observed on $LaAlO_3$ [16]. A layer-by-layer growth of SFMO on $SrTiO_3$ and MgO has also seen by Borges *et al* with corresponding deposition temperatures, but the reported magnetic and transport properties are very poor compared to the films grown at higher temperatures [15]. In addition to the growth mechanism, the choice of the substrate has been seen to affect the magnetic and magnetotransport properties of SFMO [14, 15, 17]. The saturation magnetization has been observed to decrease with larger lattice mismatch between the substrate and the SFMO, but it is also affected by the changes in deposition parameters [14, 15, 17]. The amount of antisite disorder (ASD), in which the B-site cations Fe and Mo transpose in the structure, is also affected by the choice of the substrate [17]. Various studies have connected the ASD to the saturation magnetization, Curie temperature and magnetoresistivity of SFMO thin films [14, 15, 17, 19–21].

The previous transmission electron microscopy (TEM) studies of SFMO thin films on $SrTiO_3$ have shown a sharp substrate/film interface, epitaxial growth and coherent atomic arrangements across the interface [8, 22–24]. The TEM images have also indicated that the relaxation of the SFMO thin films on $SrTiO_3$ occurs through the stacking fault formation [22, 25]. The formation of impurity phases observed by the XRD and parasitic outgrowths seen in TEM images have also suggested those as strain relief mechanisms in SFMO films [11, 16]. However, the relaxation mechanisms and interface effects have been reported only for SFMO on $SrTiO_3$ and they are still unclarified for other substrates.

Despite the numerous studies of the substrate dependent properties of SFMO thin films, the substrate induced growth and relaxation mechanisms have not been thoroughly clarified. Most of the investigations have been done with SFMO films grown at fairly low temperatures, which rarely results in optimal magnetic and magnetotransport properties. Also, the earlier TEM studies have only be carried out with SFMO films on $SrTiO_3$. In the present report, the substrate and lattice mismatch dependent growth and relaxation mechanism, substrate/film interface effects and the correlation between structural defects and magnetic properties are reported for the first time in SFMO thin films on different single-crystalline oxide substrates.

2. Experimental details

The SFMO films were made on $SrTiO_3$ (STO), $(LaAlO_3)_{0.3}(Sr_2AlTaO_6)_{0.7}$ (LSAT), $SrLaAlO_4$ (SLAO) and MgO single crystal substrates using pulsed laser deposition (PLD). These four samples were denoted as A-STO, B-LSAT, C-SLAO and D-MgO, respectively. The deposition was carried out in 9 Pa pressure Ar atmosphere and the deposition temperature was 1050 °C. The details of the film deposition are described in [18, 26] and the target preparation with sol-gel method in [27, 28]. The SFMO grows diagonally on all of these substrates. Therefore, the lattice parameter, $a_b = 5.575$ Å [29], of the bulk SFMO is compared with the diagonals of the substrate basal planes, $\sqrt{2}a_s$, to obtain the lattice mismatches,

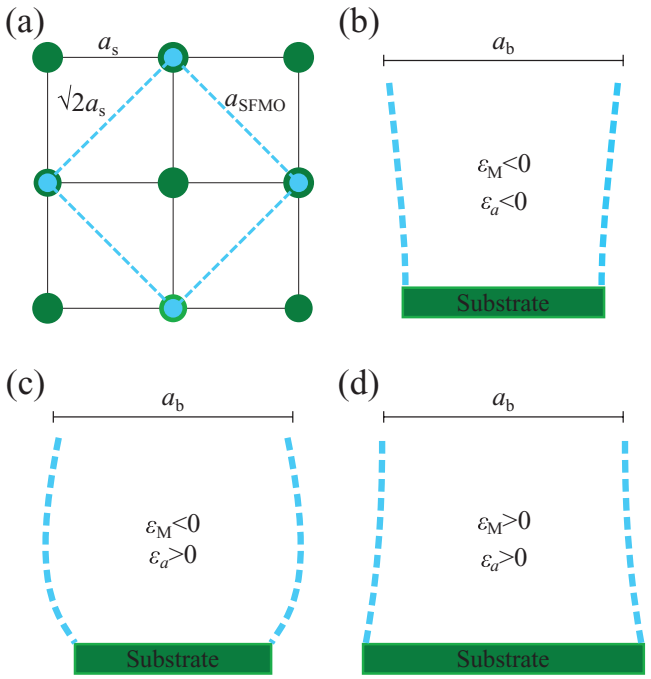

Figure 1. Schematic picture of (a) the diagonal growth of the SFMO on the substrates and (b)–(d) the strain relaxation with different lattice mismatches. The (b) demonstrates the compressive lattice mismatch resulting in compressive strain (A-STO), the (c) demonstrates the compressive mismatch resulting in tensile strain (B-LSAT and C-SLAO) and the (d) demonstrates the tensile mismatch resulting in tensile strain (D-MgO). The blue color and dotted lines represents the SFMO and the green color represents the substrate in all the figures.

Table 1. The lattice constants of the substrates and the lattice mismatches between the SFMO and the substrates.

Substrate	a_s (Å)	c_s (Å)	$\sqrt{2}a_s$ (Å)	ε_M (%)
STO	3.901		5.517	−1.05
LSAT	3.868		5.470	−1.88
SLAO	3.756	12.636	5.312	−4.71
MgO	4.214		5.964	6.97

$\varepsilon_M = (\sqrt{2}a_s - a_b)/a_b$. This is shown schematically in figure 1(a). The lattice parameters, the diagonals of the substrates basal planes and the lattice mismatches are presented in table 1.

The structural characterization was carried out with x-ray diffraction (XRD) and transmission electron microscopy (TEM). The XRD measurements were conducted using a Philips X'pert Pro MPD diffractometer in the Bragg–Brentano $\theta - 2\theta$ configuration. Also, Cu K_α radiation, Schulz texture goniometer, incident beam x-ray mirror and PIXcel detector were used in the measurements. The texture and the $2\theta - \phi$ scans were measured from the SFMO (2 0 4) peak ($2\theta = 57.106°$) and they were used together with the $\theta - 2\theta$ scans to determine the phase purity, orientation and texturing of the films. The detailed $\theta - 2\theta$ scans of the (2 0 6), (3 3 6) and (4 0 4) peaks, using different ϕ and ψ angles than for the overall $\theta - 2\theta$ scan, were used in the determination of the lattice parameters. The reciprocal space maps of all the four

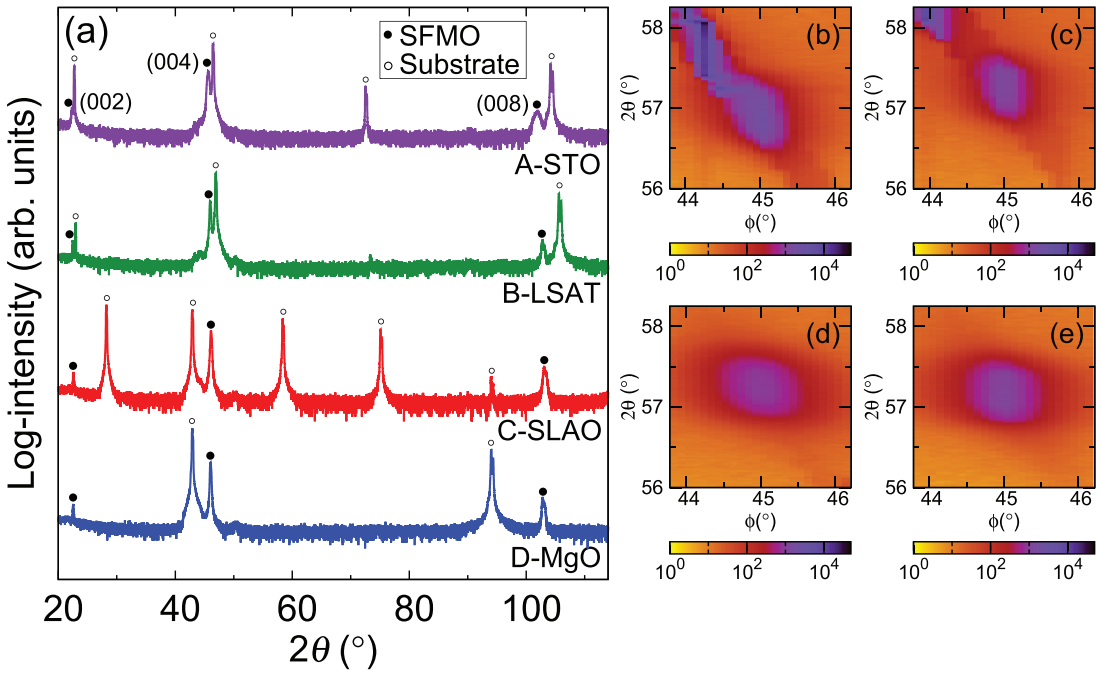

Figure 2. (a) The overall $\theta - 2\theta$ scans of the films on logarithmic scale. The open dots indicate the substrate (0 0 *l*) peaks and the full dots indicate the SFMO (0 0 *l*) peaks, which are the only visible peaks in this direction due to the epitaxial growth. The SFMO (0 0 *l*) peaks are indexed in the figure. The small peak observed near $2\theta = 50°$ comes from the sample holder. (b)–(e) The $2\theta - \phi$ scans of the SFMO (2 0 4) peak in logarithmic scale for A-STO, B-LSAT, C-SLAO and D-MgO, respectively. The substrate peak of STO and LSAT are also visible in the (b) and (c), because they are close to the SFMO peaks.

(1 0 1) and (4 0 4) peaks were also measured to obtain the ASD of the samples. In order to determine the microstructure of the films with transmission electron microscopy (TEM), focused ion beam (FIB) lamellas were prepared from all the samples. High resolution TEM (HRTEM) imaging was performed with a JEOL JEM-4010 electron microscope at an accelerating voltage of 400 kV. Also, a probe-corrected scanning TEM using high-angle annular dark field imaging (HAADF STEM) were performed with TITAN 80–300 at the voltage of 300 kV. The TEM images were also used to determine the film thicknesses, which varied between 135–145 nm for B-LSAT and 160–170 nm for A-STO, C-SLAO and D-MgO.

Quantum Design MPMS SQUID magnetometer was used in magnetic measurements. The zero field cooled (ZFC) and field cooled (FC) magnetization curves were measured up to 400 K in 0.1 T and 0.5 T fields. The Curie temperatures were determined from the $M(T)$-curves as the minimum of the temperature derivative. The hysteresis loops from −0.5 T to 0.5 T were measured at 10 K, 100 K, 300 K and 400 K as well as between −2 T and 2 T at 10 K and 100 K. In all magnetic measurements, the external magnetic field was parallel to the plane of the film, i.e. along the SFMO (0 0 1) plane.

3. Results and discussion

3.1. X-ray diffraction

The good quality of the films was confirmed with the XRD measurements. The overall $\theta - 2\theta$-scans of all the films (figure 2(a)) revealed only (0 0 *l*) peaks of the SFMO and the substrates as well as small peak from the sample holder ($2\theta = 50°$). No impurity phase peaks were observed in any of the films. The pole figures of the texture scans from the SFMO (2 0 4) peak, showed sharp peaks at the positions expected for fully textured *c*-axis oriented film.

The SFMO peaks in the overall $\theta - 2\theta$ scans (figure 2(a)) were fitted with an asymmetric gaussian function to gain the peak positions and the full width at half maxima (FWHM). Same function was also fitted to the peaks in detailed $\theta - 2\theta$ scans (not shown) to obtain the peak positions. The substrate peaks were used as an internal standard. The lattice parameters were determined with the Nelson–Riley method [30]. The (0 0 *l*) peaks were used to determine the *c* parameter and the *a* parameter was determined using (2 0 6), (3 3 6) and (4 0 4) peaks together with the obtained *c* parameter. The determined lattice parameters and the lattice parameters of the bulk SFMO ($a_b = 5.575$ Å and $c_b = 7.893$ Å [29]) were used to calculate the change in the unit cell volume, ΔV, and the substrate induced strain, $\varepsilon_a = (a - a_b)/a_b$, in *a* and in *c* directions (ε_c), respectively. These values are shown in table 2.

The in-plane strain, ε_a, is compressive only in the A-STO film and tensile in D-MgO film as expected from the lattice mismatches. In the B-LSAT and C-SLAO samples the ε_a is tensile even though the lattice mismatches are compressive. The growth of the film with compressive mismatch resulting in compressive strain (A-STO), with compressive mismatch resulting in tensile strain (B-LSAT and C-SLAO) and with tensile mismatch resulting in tensile strain (D-MgO) are schematically shown in figures 1(b)–(d). Similar behavior has been earlier observed in SFMO on LaAlO and in $La_{0.8}Ca_{0.2}MnO_3$ [16, 31], where the in-plane lattice parameters indicate that the large enough compressive mismatch leads to tensile strained

Table 2. The main structural properties of the films grown on different substrates.

Film	a (Å)	c (Å)	ΔV (%)	ε_a (%)	ε_c (%)	ε_{WH} (%)	ϕ-FWHM (°)	B_{ord}	ASD (%)
A-STO	5.554	7.941	−0.15	−0.38	0.61	0.18	0.50	0.89	11
B-LSAT	5.592	7.885	0.52	0.31	−0.10	0.02	0.51	0.96	4
C-SLAO	5.596	7.870	0.46	0.37	−0.29	0.02	0.93	0.94	6
D-MgO	5.592	7.884	0.50	0.30	−0.11	0.01	0.79	0.80	20

films. The structure of SFMO is quite closely packed, thus it is possible that the increasing compressive mismatch cannot compress the structure further. Instead, some interface defects or re-organization could occur, which over-relaxes the structure that should be compressively strained and leads to a tensile strained film. The interface defects will be discussed more detailed in the following analysis of the ϕ-FWHM values and the TEM images. The compressive mismatch, around −1%, from the STO is not large enough to result in tensile strained SFMO films. However, the −2% mismatch from the LSAT induces as large tensile strain to the SFMO film as the 7% tensile mismatch from the MgO. Thus, it can be concluded that the compressive mismatch between the SFMO and the substrate can be up to 1–2% before major structural changes occur at the interface.

The magnitudes of the in-plane strains are quite close to each other, but the sign in A-STO film is naturally opposite. The out-of-plane strain, ε_c, shows larger variation. The change in c is largest in the A-STO film, which is also seen as the smallest change in the unit cell volume. In other films, the ε_c is small and the change in the unit cell volumes are almost equal, but clearly larger. Moreover, the ε_c have an opposite sign to the corresponding in-plane strain. Thus, the decrease (increase) in a leads to increase (decrease) in c, which means that the Poisson's ratio is positive in all the films. Similar results for SFMO on STO have been reported earlier [16, 25, 32]. However, an increase in both a and c have observed in SFMO on STO by Westerburg *et al* as well as in SFMO on $LaAlO_3$ and on MgO by Jalili *et al* [16, 33]. It has also been observed, that the length of the c lattice parameter in SFMO films is affected by the deposition parameters and structural defects [16, 25, 34]. Hence, the substrate induced strain cannot alone explain the differences observed in the ΔV and the c lattice parameter.

The microstrains, ε_{WH}, of the films are shown in table 2 and they were determined from the SFMO (0 0 l) peaks with the Williamson–Hall method [35]. When the microstrain is determined from the SFMO (0 0 l) peaks, it describes the variation of the c parameter throughout the whole film thickness. In the A-STO film, the ε_{WH} is one order of magnitude larger compared to other films, which means a larger variation in the c parameter. This variation can be caused by horizontal defects like stacking faults. On the other hand, the out-of-plane strains and the change in the unit cell volumes suggest that the c parameter is elongated easier under compressive in-plane strain than compressed under tensile in-plane strain. Then the variation of the c parameter due to the relaxation is larger in compressively strained films. The observed valence fluctuation in SFMO [36, 37] together with the possible ASD and oxygen vacancies [20] could also cause variation of the lattice parameters due to the changes in ionic radii and bond lenghts and increase the microstrain, but their effect is not experimentally investigated in SFMO films. Altogether, the larger microstrain in A-STO film is more likely contributed by the larger density of stacking faults together with the c parameter variation due to the relaxation.

The ϕ-FWHMs of the SFMO (2 0 4) peaks were determined from the $2\theta - \phi$ scans and they are shown in table 2. In both A-STO and B-LSAT samples, the ϕ-FWHM is 0.5°, which corresponds very well with the earlier results of the SFMO films grown on STO substrate [14]. In C-SLAO and D-MgO samples, the ϕ-FWHM is notably larger and the value for the D-MgO also corresponds well with the earlier results [14]. The difference between the films can also be seen in the $2\theta - \phi$ scans shown in figures 2(b)–(e). The ϕ broadening is caused by the small variations in the in-plane crystal orientation due to the low angle grain boundaries, which result from the vertical dislocations in the film. When the instrumental width of ϕ determined from the substrate peak is 0.2°, the greater ϕ-FWHM values indicate that all the samples have some low angle grain boundaries. The highest low angle grain boundary density i.e. the largest amount of low angle grain boundaries is in the C-SLAO sample, in which the largest compressive mismatch results in tensile strained film. When compared to the A-STO and B-LSAT samples, the low angle grain boundary density in D-MgO film is also larger.

The ASD of the SFMO can be determined with the XRD, because the Bragg peak intensities of the superstructure depends on the ordering of the B-site atoms. The (1 0 1) of SFMO is the superstructure peak, intensity of which increases with higher B-site ordering of the SFMO [38, 39], whereas the intensity of the (4 0 4) peak does not depend on the Fe/Mo ordering. The (1 0 1)/(4 0 4) intensity ratio dependence on the B-site ordering was simulated with Fullprof Rietveld refinement program [40, 41] and is shown in figure 3(a). The antisite disorder (ASD) was determined from reciprocal space maps of all the four (1 0 1) and (4 0 4) peaks for each sample. The integrated intensities of the peaks were measured by fitting a Lorentzian peak into the ω-projection of the peaks, which includes the data of whole 2θ range (see figure 3(b)). This was done in order to be able to separate the SFMO peaks from the substrate peaks, which is a problem specially with the films on STO. After obtaining the integrated intensities of the peaks, the B-site ordering, B_{ord}, was determined from intensity ratio of (1 0 1)/(4 0 4) using a function $B_{ord} = \sqrt{I(1\,0\,1)/I(4\,0\,4)/a} + b$, where I is the integrated intensity of the peak and $a = 0.5583 \pm 0.0005$ and $b = 0.4775 \pm 0.0002$ are constants obtained from simulation

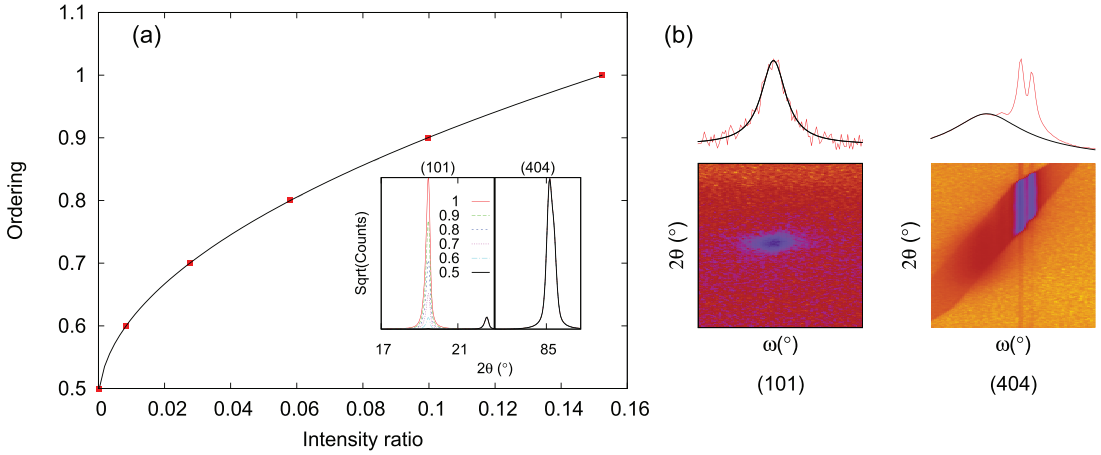

Figure 3. (a) The curve used for obtaining the antisite disorder from intensity ratio of (1 0 1)/(4 0 4) peak intensities. The inset shows the simulation at different disorder levels. The (4 0 4) peak intensity does not depend on ordering of the Fe/Mo atoms. (b) Reciprocal space maps of (1 0 1) and (4 0 4) peaks of the A-STO film on logarithmic scale. The large peaks and the background features in the (4 0 4) image arise from the substrate. Above the images are shown the ω-projections of the images from where the intensities were determined.

of the XRD intensities. It is important to measure the intensity ratios from peaks at the same tilt angle ψ so that one does not have to determine geometric corrections related to ψ in the Schulz goniometer. The geometric corrections due to different θ are taken into account in the simulation. The errors of B-site ordering were determined from the errors of the fits to the peaks and represent 99% confidence level. These errors were below 0.03 in all the samples. The level of B-site ordering and the ASD percentage are shown in table 2. The highest B-site ordering is observed in B-LSAT and C-SLAO samples in which the compressive mismatch results in tensile strained samples. In A-STO sample the ASD percentage is only slightly larger, but in D-MgO the ASD is considerably larger. However, no clear connection between other structural properties like strain or FWHM in ϕ with ASD is seen in these results.

3.2. Transmission electron microscopy

The HRTEM images of all the samples in [1 0 0] viewing direction are shown in figure 4. According to these images, all the films have sharp interface with the substrates as also seen in several previous TEM images of SFMO films grown on STO (0 0 1) or (1 1 1) substrates [8, 11, 22, 23]. Vertical defects were seen in all the samples and they are pointed out with the orange arrows in figures 4(a)–(d). In addition to the possible antiphase boundaries, it seems that at least some of these defects are threading dislocations related to the misfit dislocations at the interface. Higher magnification HAADF STEM images of the A-STO and D-MgO films showing the threading dislocation are shown as an example in figure 5(a). A Fast Fourier Transform (FFT) filtered image of the SFMO/MgO interface, obtained using (2 0 0) reflections corresponding to the in-plane direction, shows several misfit dislocations at the interface, but only some of them result in these vertical defects. As an example, close-up of the interface region in the D-MgO, together with the details of the FFT filtered image showing the misfit dislocations, are shown in figure 5(b). The misfit dislocations are rather common as a strain relaxation mechanism in these kind of heteroepitaxial systems, where a mismatch between the film and the substrate occurs. In general, a larger mismatch cause more misfit dislocations, which lead to observed threading dislocations. On the other hand, the threading dislocations are related to the low angle grain boundries, which were confirmed by the XRD studies. In the A-STO (figure 4(a)) and the B-LSAT (figure 4(b)) samples, only few these kind of vertical defects were observed. The C-SLAO (figure 4(c)) and D-MgO (figure 4(d)) samples have clearly more misfit dislocations at the interface due to larger amount of vertical defects. Hence, the density of low angle grain boundaries in these films is also higher than in the A-STO and B-LSAT films, which corresponds very well with the observed ϕ-FWHM values. According to TEM images of Ji *et al* and Fix *et al*, the strain relaxation in SFMO films occurs through defect formation. The XRD and TEM results presented here show that the defect concentration is higher in the films, which have a larger lattice mismatch. Thus, it is clear that the SFMO lattice parameters relax through defect formation at least in the films, which have large lattice mismatch between the substrate and the film.

The higher magnification HRTEM image of the D-MgO film in figure 4(e) show also sharp vertical defects in 90° angle with respect to the interface and their origin is either at the interface or close to it. These were found in all the samples as shown in figures 6(a) and (b) for the C-SLAO and D-MgO at the higher thicknesses. Figure 6(a) shows horizontal stacking fault type defects together with vertical anti-phase boundaries or dislocations, which were observed in both A-STO and C-SLAO samples. However, these horizontal defects were not observed in the B-LSAT and D-MgO films, only vertical defects were seen in the TEM images (figure 6(b)) of both samples. These horizontal defects could increase the microstrain and cause larger variation of the *c* parameter through the film. However, the XRD results are averages of the whole film and the amount of horizontal defects observed only locally is not high enough to explain the differences in microstrain and *c* parameter variation.

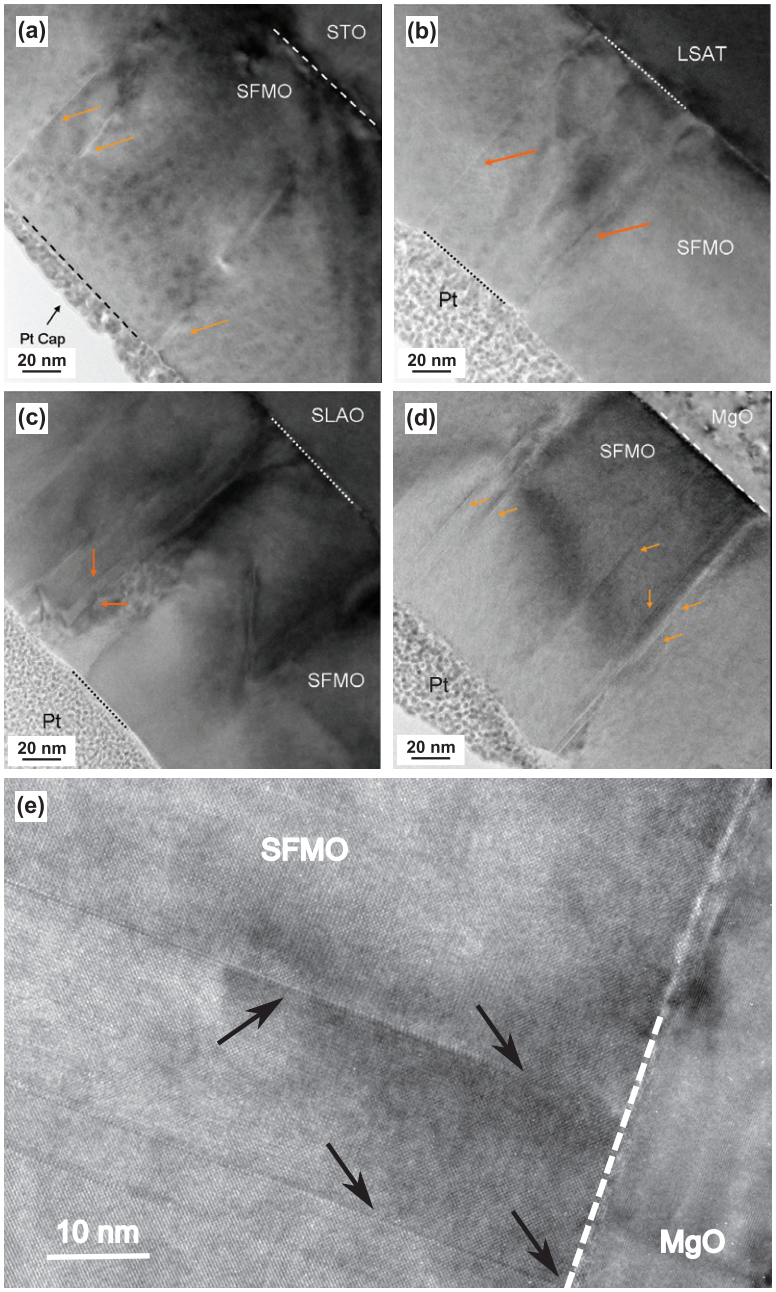

Figure 4. The HRTEM images of the (a) A-STO, (b) B-LSAT, (c) C-SLAO and (d)–(e) D-MgO in [1 0 0] viewing direction. The dotted white lines indicate the substrate/SFMO interfaces. The orange (a)–(d) and black (e) arrows point out the vertical defects such as dislocations, low angle grain boundaries and anti-phase boundaries.

The HRTEM images shown in figure 4 were also used to determine the film thicknesses. It seems that the growth rate of SFMO is similar on all the other substrates excluding the LSAT. The used 2000 pulses lead to a film thickness of 160–170 nm, which is very close to the earlier observed value of 150 nm [42]. However, the growth rate of SFMO on LSAT is lower and the film thickness of 135–145 nm is achieved with 2000 pulses. One could expect, that deposition parameters and the strain affect the film thickness. However, the lattice mismatch of LSAT is between the values for STO and SLAO and the deposition parameters were not changed between the samples. On the other hand, the results of the manganite thin films have shown that the growth rate is dependent on the orientation of the substrate and the growth mode is related to the surface instabilities of the substrate [43, 44]. This suggests that the growth rate could be related to the other properties of substrate's surface like the adhesion or the termination, which strongly affect the growth of initial layers i.e. first few unit cells) and therefore the growth mode of the film.

The HAADF STEM image of the D-MgO film in [1 1 0] direction is displayed in figure 6(c). The figure shows a particle of parasitic phase in SFMO matrix. Such particles were not observed in any other films. A higher magnification HAADF STEM images of the particle revealed its single crystalline like structure and a coherent interface with the surrounding SFMO matrix. An Energy Dispersive x-ray (EDX) spectroscopic analysis was carried out across the interface between the particle and

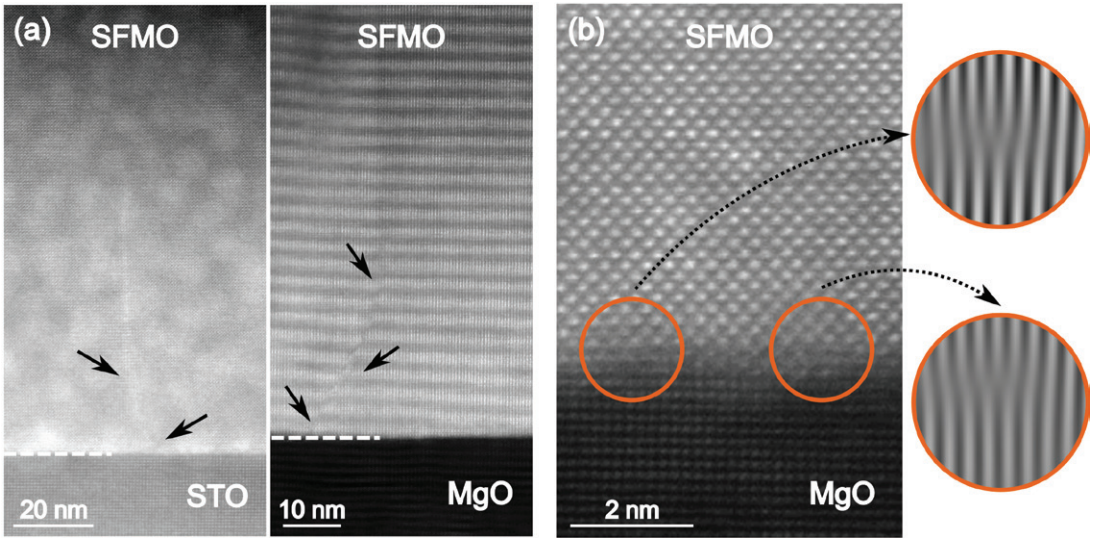

Figure 5. (a) The HAADF STEM images of the SFMO/STO and SFMO/MgO interfaces showing the threading dislocation type defects, which are caused by vertical misfit dislocations at the interface. (b) The close-up of the SFMO/MgO interface with the details from the corresponding FFT filtered image showing the misfit dislocations.

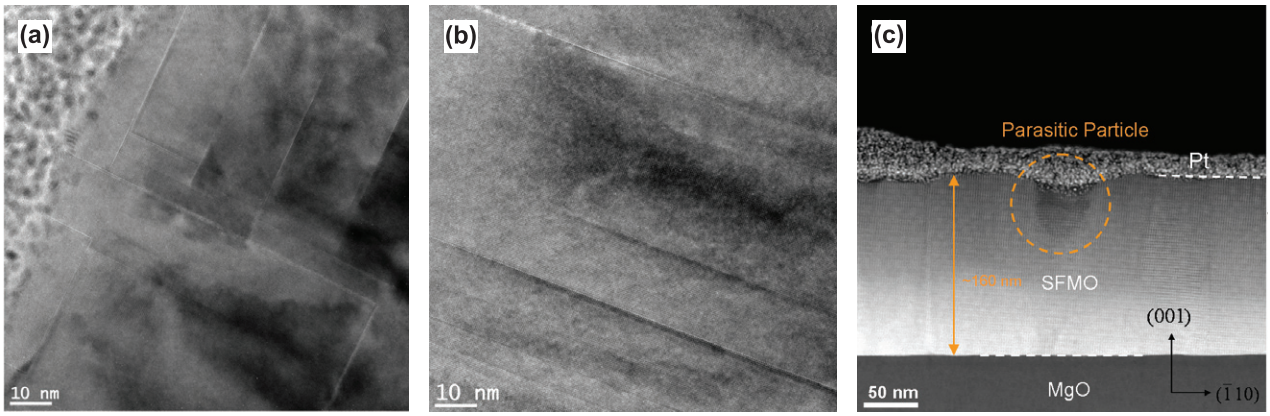

Figure 6. The higher magnification HRTEM images of (a) C-SLAO and (b) D-MgO showing the vertical anti-phase boundaries or dislocations, which were observed in all the samples. The (a) also shows the horizontal stacking fault type defects, which were observed in A-STO and C-SLAO. The both (a) and (b) images were taken at same angle relative to the substrate. (c) HAADF STEM image of the D-MgO film, which reveals the particle of parasitic phase.

SFMO matrix. Elemental analysis revealed that the particle is almost completely deficient of Fe. It most likely belongs to the $SrMoO_4$ phase, which is the most commonly observed parasitic phase in SFMO thin films [45]. However, parasitic phases were not observed with XRD, which means that the amount of impurity is below the XRD detection limit. This kind of parasitic phase has been earlier observed in the TEM images of SFMO on STO [45]. Also, evidence for an iron based outgrowths has been reported [11]. The coherent interface between the SFMO matrix and the parasitic particle together with the largest lattice mismatch in D-MgO suggest that the formation of the parasitic particle is not related to the laser-target interaction originated droplet, but could be connected to the growth process of the vaporized species induced by the large tensile strain.

3.3. Magnetic properties

The effect of lattice mismatch induced structural defects on the magnetic properties of the films on different substrates were investigated using field and temperature dependent magnetization measurements. Magnetic hysteresis loops measured at 10 K are shown in figure 7(a) for all the samples. The dia- and paramagnetic effects from the substrate and the sample holder have been eliminated from the results. The saturation magnetization, M_s, the remanence, M_r, and the coercivity field, B_c, at 10 K were determined from the hysteresis loops and they are shown in table 3. The shape of the $M(B)$-hysteresis curve at 10 K for A-STO is as expected for a typical ferromagnet with a high remanence of 63% of saturation magnetization and a coercivity field of 34 mT. The hysteresis loops of B-LSAT and D-MgO are slightly skewed with remanence 28% of M_s and in the C-SLAO the skeweness of the hysteresis loop is significant with remanence being only 15% of the M_s. The field required for saturation of the magnetization in A-STO, B-LSAT and D-MgO is visible in figure 7(a) and remains fairly constant. However, the hysteresis loops measured up to 2 T revealed that magnetization of C-SLAO saturates in considerably larger fields. These changes are most likely

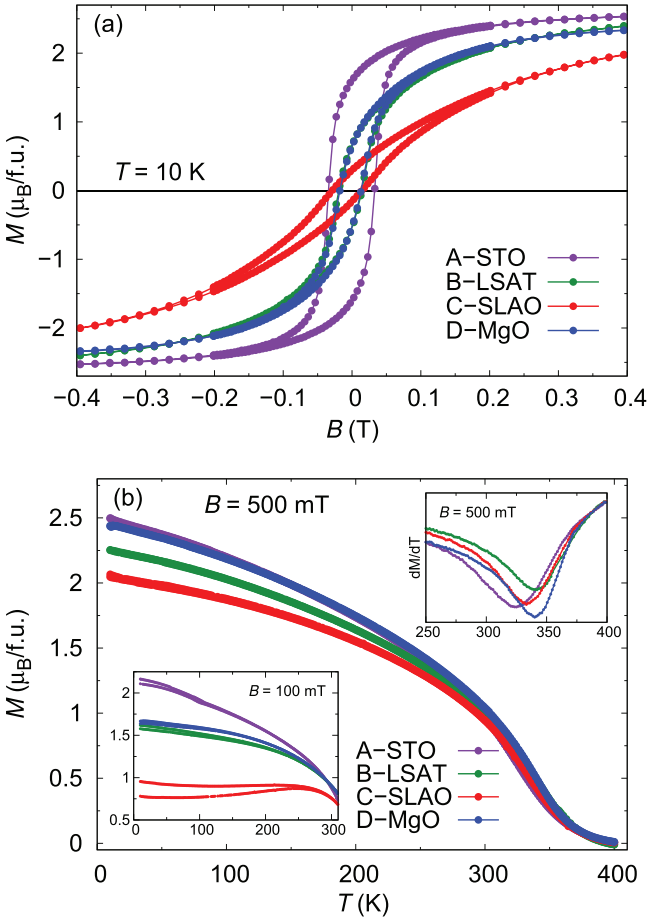

Figure 7. (a) The magnetization hysteresis loops at 10 K for all the samples. The curves for B-LSAT and D-MgO are on top of each other. (b) The temperature dependence of the magnetization in 500 mT field. The bottom left inset shows the low temperature close-up of the irreversibility between ZFC and FC magnetization curves measured in 100 mT field. The top right inset shows the temperature derivative of the magnetization in 500 mT. The effect of substrate and the sample holder are subtracted from all the curves.

Table 3. The main magnetic properties of the films grown on different substrates.

Film	T_C (K)	M_s 10 K (μ_B f.u.$^{-1}$)	B_c 10 K (mT)	M_r 10 K (μ_B f.u.$^{-1}$)
A-STO	324	2.54	34	1.61
B-LSAT	340	2.34	17	0.66
C-SLAO	335	2.00	21	0.30
D-MgO	337	2.33	15	0.65

due to the difference in the defect concentration in the films, since the defects cause domain wall formation and pinning. Thereby, the field required to modify and align the domains is different depending on the density of defects. According to the observed ϕ-FWHM and the TEM images, the C-SLAO contains most low-angle grain boundaries and other defects such as dislocations and stacking faults, which cause the skeweness of the hysteresis loop. Similar defect and grain boundary induced broadness of para-ferromagnetic transition and domain wall pinning was previously seen in half-metallic oxide $La_{0.7}Sr_{0.3}MnO_3$ [46, 47].

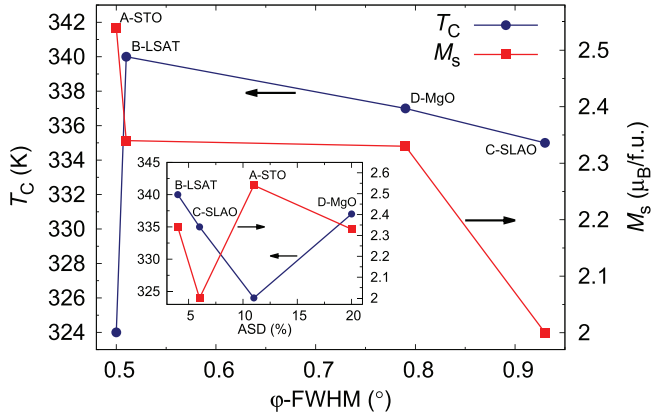

Figure 8. The Curie temperature (left hand scale) and the saturation magnetization (right hand scale) as a function of ϕ-FWHM, which describes the amount of low angle grain boundaries in the samples. The absolute value of the lattice mismatch increases as the ϕ-FWHM. The inset shows the Curie temperature (left hand scale) and the saturation magnetization (right hand scale) as a function of ASD. The samples are labelled in the figure, because the ϕ-FWHM and the ASD do not correspond in the films.

Major differences in M_s and B_c were not observed between the SFMO films on different substrates. However, the absolute M_s values are affected by the accuracy of the film thickness determination. The largest saturation magnetization of 2.54 μ_B f.u.$^{-1}$and the highest coercivity field of 34 mT were observed in A-STO film. Also, both the M_s and B_c are almost equal in B-LSAT and D-MgO samples. In C-SLAO the coercivity field is slightly larger compared to the B-LSAT and D-MgO, but it has the lowest saturation magnetization of 2 μ_B f.u.$^{-1}$. The observed saturation magnetization values are almost half of the theoretical value of 4 μ_B f.u.$^{-1}$, but similar values for SFMO thin films have been reported earlier [9, 14]. The low M_s value has been previously connected to the ASD in SFMO thin films [15, 19, 20, 48]. The antisite occupancy of Mo at Fe positions modify the magnetic exchange interaction. Sánchez *et al* showed that due to changed positions of Fe and Mo atoms, strong Fe–O–Fe superexchange interactions take place that give rise to the antiferromagnetic (AFM) ordering of the Fe spins reducing the saturation moment [49]. Since the XRD measurements confirmed that all the films have some ASD, it is clear that the saturation magnetization values are not as high as the theoretical value. If increasing ASD is considered as the main factor for reduced magnetization, our M_s values suggest that the best B-site ordering is achieved with SFMO on STO and the largest ASD on the samples on SLAO. However, this is inconsistent with the measured ASD values presented in table 2. Earlier, M_s has shown linear dependence of the ASD [20, 48, 50], whereas our results presented at the inset of figure 8 do not show clear correlation between the ASD and M_s. Thus, it is clear that the ASD is not the only reason for decreased saturation moment in SFMO. The M_s dependence on the ϕ-FWHM (figure 8) shows that the M_s has a decreasing overall tendency with increasing ϕ-FWHM, which suggests that the saturation magnetization is more dependent on the other structural defects like low angle grain

boundaries, dislocations and stacking faults. However, the M_s values for B-LSAT and D-MgO are similar, despite the quite large change in the ϕ-FWHM. On this basis, the possible contribution of the tensile lattice mismatch and other defects like oxygen vacancies cannot be totally neglected. Several theoretical studies have indicated that the oxygen vacancies in SFMO reduce the saturation magnetization [51–54]. It was experimentally shown before that oxygen deficiency can lead to longer Fe/Mo–O bonds due to the displacement of Fe/Mo atoms from the oxygen vacancy and also reduced Fe/Mo–O–Fe/Mo bond angle compared to the ideal value of 180° [55]. These together with the observed dislocations can lead to the modified exchange interaction, which would affect the magnetic ordering and can lead to a reduced M_s. It is also possible that the low angle grain boundaries and dislocations promote the formation of oxygen vacancies in SFMO thin films.

The temperature dependence of magnetization in 500 mT is shown in figure 7(b) and the bottom left inset shows the low temperature part of the ZFC and FC magnetization curves measured in 100 mT. The shape of the ferro-paramagnetic transition in 500 mT field, which is high enough for saturation, is similar in all the samples. The ZFC and FC curves for the A-STO, B-LSAT and D-MgO do not show any deviation unlike earlier observed for SFMO films on STO [26]. However, the 100 mT magnetization curve of C-SLAO differs strongly from the others as already expected from the shape of the hysteresis loops. The ZFC and FC curves deviate at around 250 K, whereas earlier the irreversibility in films grown on STO has been observed only below 100 K [26]. The irreversibility of C-SLAO is caused by the domain wall pinning in SFMO thin film defects, which was also seen as a skeweness of the $M(B)$ hysteresis. It is also possible that defects cause some distortions in atomic bond geometry, which could contribute the observed irreversibility.

The temperature dependence of magnetization in 500 mT was also used to determine the Curie temperatures, T_C's, of the films. The onset Curie tempertures, which are determined from the point where the magnetization deviates from the minimum, are almost equal around 390 K in all the films. Therefore, the T_C values were obtained as the minimum of the temperature derivative of magnetization, which are presented at the top right inset of figure 7(b) and the values are listed in table 3. In tensile strained films, the T_C is approximately 340 K and in A-STO the T_C is 324 K, which suggests that the Curie temperature depends on the direction of the strain. However, the nature of the ferro-paramagnetic transition is also affected by the low angle grain boundaries and other defects observed in the XRD and TEM results. The Curie temperature as a function of ϕ-FWHM in figure 8 shows a slight decrease in T_C with increased amount of these defects in tensile strained samples, but it cannot explain the lower T_C in compressively strained A-STO. However, the Curie temperature is also affected by the ASD and oxygen vacancies. Monte Carlo simulation study of SFMO by Ogale *et al* [20] has proposed a decrease in T_C with increasing ASD, but they did not study the effect of oxygen vacancies. This connection between the ASD and T_C would mean that the A-STO, which has the lowest T_C, has the largest ASD. If the D-MgO sample is ignored, this is also the case in our samples as seen from the inset of figure 8. The A-STO film has higher ASD and lower T_C than the B-LSAT and C-SLAO films in which both the ASD and T_C are almost equal. When the T_C of the D-MgO sample is taken into account, the ASD alone cannot explain the differences between tensile strained and compressively strained samples. In manganites, the T_C has been seen to decrease with the oxygen vacancies due to the decrease in number of Mn^{3+}–Mn^{4+} pairs, which cause a reduction of the transfer interaction of e_g electrons [56, 57]. However, theoretical calculations have shown that the T_C of SFMO is increased with oxygen vacancies [51]. Due to the absence of oxygen, the antiferromagnetic coupling between Fe–Mo is increased. This strengthens the Fe–Mo mediated ferromagnetic coupling between the Fe–Fe and leads to an increase in T_C. Unfortunately, previous experimental investigations about the effect of oxygen vacncies on the T_C of SFMO was not found, which is most likely due to the sensitivity of SFMO on deposition atmosphere and the easily formed impurities with additional oxygen [11, 26, 33, 58]. On the other hand, the Curie temperature of SFMO has been seen to decrease with elongation of the c-axis [34], which happens in the A-STO. Thus, it is possible that the tensile strain and the observed defects promote the formation of oxygen vacancies and cause the higher T_C compared to compressively strained A-STO. The higher oxygen vacancy concentration in tensile strained samples is also in good agreement with the observed changes in the saturation magnetization. Altogether, the magnetic properties of the SFMO films are highly dependent on the choice of the substrate through lattice mismatch induced structural defects observed with the XRD and TEM. The low angle grain boundaries and dislocations promote the pinning sites for the domain motion and rotation as well as could advance the formation of the oxygen vacancies.

4. Conclusions

To conclude, epitaxial SFMO thin films on different substrates show lattice mismatch induced growth defects that have significant impact on the magnetic properties of the films. It was found that the choice of the substrate has a crucial role in the growth, microstructure and magnetic properties of SFMO thin films through lattice mismatch induced defects. The high enough compressive mismatch was seen to result in tensile strained films and the limit for compressive mismatch without major structural changes at the interface is between 1–2%. In all the samples, indications of the low angle grain boundaries, dislocations and stacking faults were found and their amount increased with larger lattice mismatch. This indicates that the lattice parameters of SFMO relax through defect formation at least when the lattice mismatch is high enough. The films with compressive mismatch

were found to be phase pure, fully textured and *c*-axis oriented, but a small $SrMoO_4$ parasitic particle was found in the film on MgO.

The magnetic properties of the films are highly dependent on the choice of the substrate through the interface defects. The $M(B)$ hysteresis curves were skewed and the remanence was reduced by increasing the amount of defects, which act as a pinning sites for domain motion and rotation. Even though the observed ASD reduces the T_C and the M_s, it was found to be outshined by the larger effect of the lattice mismatch induced defects. The higher T_C in tensile strained films and the differences in saturation magnetization suggest that the tensile strain and the interface defects promote the formation of oxygen vacancies, which increase the T_C and reduce the M_s. According to these results, the interface defects have larger role in the magnetic properties of SFMO than the ASD. The low angle grain boundaries, dislocations and stacking faults together with the tensile strain can promote the formation of oxygen vacancies as well as dramatically change the $M(B)$ hysteresis behavior, the Curie temparature and the saturation magnetization. Therefore, the choice of substrate needs to be considered when fabricating SFMO thin films to be used in novel spintronic applications.

Acknowledgment

We thank Professor D Hesse for valuable discussions and Mr N Schammelt for the FIB-based TEM sample thinning work of our SFMO thin films. The Jenny and Antti Wihuri Foundation and the Magnus Ehrnrooth Foundation are acknowledged for financial support.

References

[1] Kobayashi K I, Kimura T, Sawada H, Terakura K and Tokura Y 1998 *Nature* **395** 677
[2] Yamaguchi T, Suwaki H, Kikuta K and Hirano S 2005 *Solid State Commun.* **133** 71
[3] Suwaki H, Yamaguchi T, Sakamoto W, Yogo T, Kikuta K and Hirano S 2005 *J. Magn. Magn. Mater.* **295** 230
[4] Zhu X B, Dai J M, Li X H, Zhao B C, Liu S M, Song W H and Sun Y P 2005 *Mater. Lett.* **59** 2366
[5] Rager J, Berenov A V, Cohen L F, Branford W R, Bugoslavsky Y V, Miyoshi Y, Ardakani M and MacManus-Driscoll J L 2002 *Appl. Phys. Lett.* **81** 5003
[6] Boucher R 2005 *J. Phys. Chem. Solids* **66** 1020
[7] Boucher R 2006 *J. Magn. Magn. Mater.* **301** 251
[8] Hauser A J, Williams R E A, Ricciardo R A, Genc A, Dixit M, Lucy J M, Woodward P M, Fraser H L and Yang F 2011 *Phys. Rev.* B **83** 014407
[9] Manako T, Izumi M, Konishi Y, Kobayashi K I, Kawasaki M and Tokura Y 1999 *Appl. Phys. Lett.* **74** 2215
[10] Paturi P, Huhtinen H, Laiho R and Raittila J 2001 *IEEE Trans. Appl. Supercond.* **11** 3449
[11] Besse M, Pailloux F, Barthelemy A, Bouzehouane K, Fert A, Olivier J, Durand O, Wyczisk F, Bisaro R and Contour J P 2002 *J. Cryst. Growth* **241** 448
[12] Santiso J, Figueras A and Fraxedas J 2002 *Surf. Interface Anal.* **33** 676
[13] di Trolio A, Larciprete R, Testa A M, Fiorani D, Imperatori P, Turchini S and Zema N 2006 *J. Appl. Phys.* **100** 013907
[14] Saloaro M, Majumdar S, Huhtinen H and Paturi P 2012 *J. Phys.: Condens. Matter* **24** 366003
[15] Borges R P, Lhostis S, Bari M A, Versluijs J J, Lunney J G, Coey J M D, Besse M and Contour J P 2003 *Thin Solid Films* **429** 5
[16] Jalili H, Heinig N F and Leung K T 2010 *J. Chem. Phys* **132** 204701
[17] Kumar D and Kaur D 2010 *Physica* B **405** 3259
[18] Suominen T, Raittila J and Paturi P 2009 *Thin Solid Films* **517** 5793
[19] Fix T, Versini G, Loison J L, Colis S, Schmerber G, Pourroy G and Dinia A 2005 *J. Appl. Phys.* **97** 024907
[20] Ogale A S, Ogale S B, Ramesh R and Venkatesan T 1999 *Appl. Phys. Lett.* **75** 537
[21] Singh V N and Majumdar P 2011 *Europhys. Lett.* **94** 47004
[22] Ji W J, Xu J, Zhang S T, Chen Y, Zhou J, Gu Z-B, Yao S-H and Chen Y F 2013 *Solid State Commun.* **163** 28
[23] Wang S, Pan H, Zhang X, Lian G and Xiong G 2006 *Appl. Phys. Lett.* **88** 121912
[24] Xu J, Ji W J, Wang J F, Gu Z B and Zhang S T 2014 *Ceram. Int.* **40** 4485
[25] Fix T, Stoeffler D, Colis S, Ullhaq C, Versini G, Vola J P, Huber F and Dinia A 2005 *J. Appl. Phys.* **98** 023712
[26] Paturi P, Metsänoja M and Huhtinen H 2011 *Thin Solid Films* **519** 8047
[27] Raittila J, Salminen T, Suominen T, Schlesier K and Paturi P 2006 *J. Phys. Chem. Solids* **67** 1712
[28] Suominen T, Raittila J, Salminen T, Schlesier K, Linden J and Paturi P 2007 *J. Magn. Magn. Mater.* **309** 278
[29] Nakamura S and Oikawa K 2003 *J. Phys. Soc. Japan* **72** 3123
[30] Nelson J B and Riley D P 1945 *Proc. Phys. Soc.* **57** 160
[31] Rao R A, Lavric D, Nath T K, Eom C B, Wu L and Tsui F 1999 *J. Appl. Phys.* **85** 4794–6
[32] Venimadhav A, Sher F, Attfield J P and Blamire M G 2004 *J. Magn. Magn. Mater.* **269** 101
[33] Westerburg W, Reisinger D and Jakob G 2000 *Phys. Rev.* B **62** R767
[34] Sánchez D, García-Hernández M, Auth N and Jakob G 2004 *J. Appl. Phys.* **96** 2736
[35] Birkholz M 2006 *Thin Film Analysis by X-Ray Scattering* (Weinheim: Wiley)
[36] Lindén J, Yamamoto T, Karppinen M and Yamauchi H 2000 *Appl. Phys. Lett.* **76** 2925
[37] Navarro J, Fontcuberta J, Izquierdo M, Avila J and Asensio M C 2004 *Phys. Rev.* B **70** 054423
[38] Park B J, Han H, Kim J, Kim Y J, Kim C S and Lee B W 2004 *J. Magn. Magn. Mater.* **272–6** 1851
[39] Balcells L, Navarro J, Bibes M, Roig A, Martinez B and Fontcuberta J 2001 *Appl. Phys. Lett.* **78** 781
[40] Rodriguez-Carvajal J 1990 *Abstracts of the Satellite Meeting on Powder Diffraction of the XV Congress of the IUCr* p 127
[41] Rodriguez-Carvajal J 1993 *Physica* B **192** 55
[42] Saloaro M, Majumdar S, Huhtinen H and Paturi P 2013 *EPJ Web Conf.* **40** 15012
[43] Majumdar S, Kooser K, Elovaara T, Huhtinen H, Granroth S and Paturi P 2013 *J. Phys.: Condens. Matter* **25** 376003
[44] Fu M, Xie Q, Gu M, Zhang Y, Wu X, Pan F, Chen X, Wu L, Pan G and Gao J 2010 *J. Cryst. Growth* **312** 1617
[45] Deniz H, Preziosi D, Alexe M, Hesse D, Eisenschmidt C, Schmidt G and Pintilie L 2015 *J. Mater. Sci.* **50** 3131

[46] Majumdar S, Huhtinen H, Majumdar H and Paturi P 2012 *J. Alloys Compd.* **512** 332
[47] Majumdar S, Huhtinen H, Paturi P and Majumdar H S 2013 *J. Mater. Sci.* **48** 2115
[48] Balcells L, Navarro J, Bibes M, Roig A, Martinez B and Foncuberta J 2001 *Appl. Phys. Lett.* **78** 781
[49] Sanchez D, Alonso J A, Garcia-Hernandez M, Martinez-Lope M J, Martinez J L and Mellergård A 2002 *Phys. Rev.* B **65** 104426
[50] Venimadhav A, Vickers M E and Blamire M G 2004 *Solid State Commun.* **130** 631
[51] Hoffmann M, Antonov V N, Bekenov L V, Kokko K, Hergert W and Ernst A 2015 arXiv:1504.02629
[52] Stoeffler D and Colis S 2005 *J. Phys.: Condens. Matter* **17** 6415
[53] Stoeffler D and Colis S 2006 *Mater. Sci. Eng.* B **126** 133
[54] Mishra R, Restrepo O D, Woodward P M and Windl W 2010 *Chem. Mater.* **22** 6092
[55] Sher F, Williams A J, Venimadhev A, Blamire M G and Attfield J P 2005 *Chem. Mater.* **17** 1792
[56] Abdelmoula N, Guidara K, Cheikh-Rouhou A, Dhahri E and Joubert J C 2000 *Solid State Chem.* **151** 139
[57] Dhahri R and Halouni F 2004 *J. Alloys Compd.* **385** 48
[58] Töpfer J, Kircheisen R and Barth S 2009 *J. Appl. Phys.* **105** 07D712